Separation and Purification Technology 355 (2025) 129588

Contents lists available at ScienceDirect

Separation and Purification Technology

journal homepage: www.elsevier.com/locate/seppur

Unidirectional ice-templating for aerogel adsorbents: Excellent pore structure and high CO_2 capture performance for direct air capture

Hao Dong [a], Tao Wang [a,*], Fengsheng Liu [a], Zhongyang Luo [a], Xiang Gao [a,b], Ming Cai [c]

[a] State Key Laboratory of Clean Energy Utilization, Zhejiang University, Hangzhou 310027, China
[b] Key Laboratory of Clean Energy and Carbon Neutrality of Zhejiang Province
[c] Xi'an Thermal Power Research Institute Co., LTD

ARTICLE INFO

Editor: Dr. S Yi

Keywords:
Direct air capture
Aerogel
Pore structure
Kinetic analysis
Moisture swing adsorbents

ABSTRACT

The ultralow atmospheric partial pressure of CO_2 (~40 Pa) presents a significant challenge for direct air capture (DAC). In this study, high-performance porous aerogel adsorbents are prepared using the unidirectional freezing–ice-templating method. The dispersion of the mixed solution is effectively improved by particle size modulation, and functionalized materials with abundant gas channels are constructed by the rapid cooling of liquid N_2. The adsorbents feature a cross-structure comprising monolayer active components and nanoscale layered carriers. The unique micro/mesoporous composite structure of the adsorbents facilitates gas-phase transport. When the functional group efficiency is increased by 5.8 times, the prepared adsorbents demonstrate excellent CO_2 capture capacity (1.17 mmol/g and 148 mol/m^3) and a low adsorption half-time (1.28 min). The unique cross-structure of the adsorbents renders them hydrophobic; thus, they show higher adsorption capacity at high humidity than other moisture swing adsorbents. At the molecular scale, quantum chemical calculations show that appropriate coordination between the active components and carriers enhance the water vapor hindering ability of the adsorbents. The developed aerogel adsorbents significantly expand the application scenarios for moisture swing adsorbents and enhance the efficiency of DAC.

1. Introduction

Given the contribution of greenhouse gas emissions, particularly CO_2, to global warming, efforts to reduce CO_2 emissions cannot be delayed. The development of negative-emission technologies is necessary to limit the global temperature rise to 1.5 ℃ [1,2]. Direct air capture (DAC) is important to effectively capture CO_2 from mobile sources. DAC offers advantages such as low environmental risk, low land demand, and substantial potential for emission reduction. The Intergovernmental Panel on Climate Change report "Climate Change 2022 Mitigation of Climate Change" stated that DAC has the potential to capture nearly 100 billion tons of CO_2 by the end of this century [3]. Similarly, in 2022, the International Energy Agency released a special report on DAC, recognizing it as "a key technology for net-zero emissions" [4].

The ultralow atmospheric partial pressure (P/P_0) of CO_2 (~40 Pa) poses a significant kinetic challenge in capturing CO_2 directly from ambient air [5]. Natural processes, such as photosynthesis and ocean CO_2 uptake, capture CO_2 from the atmosphere at very low rates of 10^{-6} and 10^{-8} mol/(m^2 s^1), respectively [6]. The kinetics of CO_2 adsorption using artificial materials based on DAC technology can be hundreds of times higher than that of natural procedures. Earlier DAC materials, such as alkaline metal oxides [7], alkaline metal hydroxides [8], amine solutions [9], and solid amines [10–13], were usually used for flue gas capture. Alkaline metal-based absorbents have been widely implemented in commercial applications. However, further research is needed to address the high temperatures required for the regeneration of these absorbents [14]. Recent studies have demonstrated that solid amines can be used for adsorption with lower exergy consumption, offering a potential alternative [15]. It is also crucial to prevent the oxidative degradation of solid amine adsorbents [16]. Both alkaline metal-based absorbents and solid amine adsorbents have high heat requirements. The moisture-swing adsorption (MSA) process, which utilizes quaternary ammonium (QA) adsorbents, presents a promising solution to the challenges of high heat demand and material instability [17,18]. In the MSA procedure, CO_2 adsorption occurs under low humidity conditions, while desorption takes place in high humidity environments, typically at 100 % RH.

* Corresponding author.
E-mail address: oatgnaw@zju.edu.cn (T. Wang).

https://doi.org/10.1016/j.seppur.2024.129588
Received 18 June 2024; Received in revised form 4 September 2024; Accepted 5 September 2024
Available online 7 September 2024

In recent years, interest in DAC materials with porous structures has grown, as such materials provide molecular transport channels that are essential for both the functionalization of the active substrate and the CO_2 adsorption process [6,19,20]. Functionalization is commonly achieved through impregnation, grafting, and in situ polymerization. Previous studies revealed that amine molecules, owing to their high surface potential, tend to selectively occupy smaller pores (typically < 10 nm) during impregnation [21,22]. However, this phenomenon results in complete pore-filling, which hampers CO_2 transport, particularly in adsorbents with predominantly microporous structures. The use of adsorbents primarily composed of mesoporous and macroporous materials, such as aerogels, mesoporous alumina, and mesoporous silica, is recommended to overcome this limitation.

Aerogels are porous materials with a three-dimensional hierarchical network structure, including macropores, mesopores, and micropores [23]. Considering its low density, high specific surface area, controllable pore size, and good stability, aerogels have been used by some researchers as backbone materials for porous DAC adsorbents. Shi et al. [24] proposed a chitosan-based aerogel adsorbent with a CO_2 adsorption capacity of 0.18 mmol/g at 30 ℃, along with an adsorption half-time ($t_{1/2}$) of 7 min. As an active substrate for aerogel adsorbents, the quaternary ammonium functional group is characterized by low energy consumption owing to its moisture swing adsorption ability; specifically, this functional group utilizes moisture swing instead of heat or electrical energy to achieve CO_2 adsorption/desorption [25]. Previous studies on moisture swing adsorbents have focused more on enhancements in their CO_2 adsorption capacity than on their kinetics [26]. Hou et al. [27] prepared quaternized cellulose (QCL) with a CO_2 $t_{1/2}$ of 9.8 min at room temperature. Wang et al. [6] developed a predominantly mesoporous QA resin adsorbent and reported a $t_{1/2}$ of 2.9 min, which was the lowest value reported at that time. Porous adsorbents for the removal of other acid gases are also of concern. Kan et al. [28] recently proposed a foamed Ce-MOF single crystals designed from a multiscale co-assembly. The adsorbent possessed well defined microporous tandem-ordered *meso*-macroporous foams. It delivered exceptional performance than many other adsorbents in terms of the high-temperature reversible adsorption and separation of SO_2.

This study addresses the kinetic challenges of DAC adsorbents brought about by ultralow CO_2 P/P_0 by preparing aerogel adsorbents using the freezing–ice-templating method with QCL and macroporous ion-exchange resin (IRA) powder as active substrates. We explored the synthesis of QCL and analyzed the effects of the etherizer dosage and reaction time. The effect of substrate dosage on the aerogel adsorbents as well as their CO_2 adsorption capacity at 400 ppm CO_2 and different relative humidities (RHs) were also explored. The peak adsorption capacity of the adsorbents demonstrated a unique phenomenon in the medium-humidity range. Variations in the water vapor hindering ability of the different aerogel adsorbents were compared using macroscopic and microscopic simulations. In addition, the mechanism of the H_2O effect during CO_2 adsorption was proposed. The QCL- and IRA-based aerogel adsorbents were characterized using Fourier transform infrared spectrometry (FTIR), scanning electron microscopy (SEM), N_2 adsorption–desorption (Brunauer–Emmett–Teller [BET]) analysis, static H_2O contact angle tests, and H_2O isothermal adsorption analysis. The aerogel adsorbents synthesized in this study provide an effective strategy for CO_2 capture in wet environments (50 %–80 % RH) while maintaining high CO_2 adsorption capacity and kinetics.

2. Materials and methods

2.1. Materials

QA cross-linked polystyrene (PS) resin was purchased from Rhawn Reagent Co., Ltd. Polyvinyl alcohol (PVA) was purchased from National Pharmaceutical Group Chemical Reagent Co., Ltd. The alcoholysis degree of PVA was 99 % and the degree of polymerization was 1700. The resins were purified according to standard procedures and then dried at 70 ℃ for 8 h. The pretreated IRA particles were pulverized by mechanical stirring and sorted using a 200-mesh (d=75 μm) sieve tray. Liquid N_2, high-purity N_2, and CO_2 were obtained from Jingong Special Gas Company. The deionized (DI) water used in the experiments was prepared in the laboratory.

Glycidyl trimethyl ammonium chloride (GTMAC) was purchased from Aladdin. Sodium chlorite was purchased from Macklin. Cellulose was obtained from poplar wood as the biomass raw material, purified, crushed, sieved to 80–100 mesh, and dried overnight at 105 ℃. The method of Hu et al. [29,30] was used to purify the cellulose and successively remove lignin and hemicellulose from the biomass raw materials; Fig. S1 shows the steps for this process.

2.2. Fabrication of QCL or IRA aerogels

Material preparation. IRA powder was dipped in a 1 M Na_2CO_3 aqueous solution for 2 d for complete ion exchange and then dried at 40 ℃. Cellulose was quaternized according to the method of Marc et al. [31]. Specifically, 5 g of purified cellulose was placed in 100 mL of 4 wt % NaOH and left to rest overnight. A certain amount of GTMAC (2.9, 5.8, or 8.7 g/g CL) as the etherizer was added to the mixture and reacted at 65 ℃ for 9, 18, or 27 h (Fig. 1a). The reaction product was pumped and filtered, ion-exchanged using the same procedure as that for IRA powder, and dried at 40 ℃ for further use [32]. A certain amount of PVA was added to DI H_2O at 95 ℃ to prepare a 1 wt% solution.

Aerogel fabrication. The aerogels were fabricated as shown in Fig. 1b. The solid content of the active component was 2 %. QCL or IRA and DI H_2O were added to a beaker, followed by 1 wt% PVA solution, which was added according to the required ratio (active component weight = 50, 70, and 90 wt%), and mixed. The mixture was evenly dispersed by ultrasonication for 15 min and transferred a polytetrafluoroethylene (PTFE) mold. The PTFE mold was placed on a Cu plate in a stainless-steel container. Liquid N_2 was poured into the container until the solution in the mold was completely frozen, and the mold was transferred to a freeze-dryer. Lyophilization was performed for 72 h to obtain the aerogels.

2.3. Characterization methods

The cellulose content of poplar wood was measured using the Van–Soest method. A vario EL cube elemental analyzer was used to determine the C, H, and N contents of the samples. SEM images were acquired using a Hitachi SU8010 instrument. Elemental distributions were analyzed using an X-Max 80 energy dispersive spectrometer (EDS, Oxford Diffraction, Co., Ltd., England). N_2 physisorption experiments were performed on a Micrometrics ASAP2460 instrument at 77 K. Surface areas were estimated using the BET method, and the data were obtained at P/P_0 ranging from 0.05 to 0.3. Pore volumes were estimated from the total N_2 sorption at a P/P_0 of 0.99. Pore size distributions were estimated using the nonlocal density functional theory (NLDFT) model. A Nicolet iS20 FTIR spectrometer (Thermo Scientific) equipped with an attenuated total reflectance (ATR) accessory was used to collect FTIR spectra. Densities were measured using a DMA 4200 M density meter (Anton Paar). The static H_2O contact angles of the materials were measured using a Dataphysics OCA20 instrument. This test was repeated three times to obtain the average contact angle·H_2O equilibrium adsorption capacities were measured using a BELSORP Max II instrument (Japan) based on gravimetric analysis. Calorimetric curve was measured by Differential Scanning Calorimetry (DSC, TA Q2000-DSC2500, Co., Ltd., USA).

2.4. CO_2 adsorption/desorption measurements

The CO_2 adsorption/desorption tests were performed in a fixed-bed reactor (Fig. S2). First, the airtightness of the reaction device was

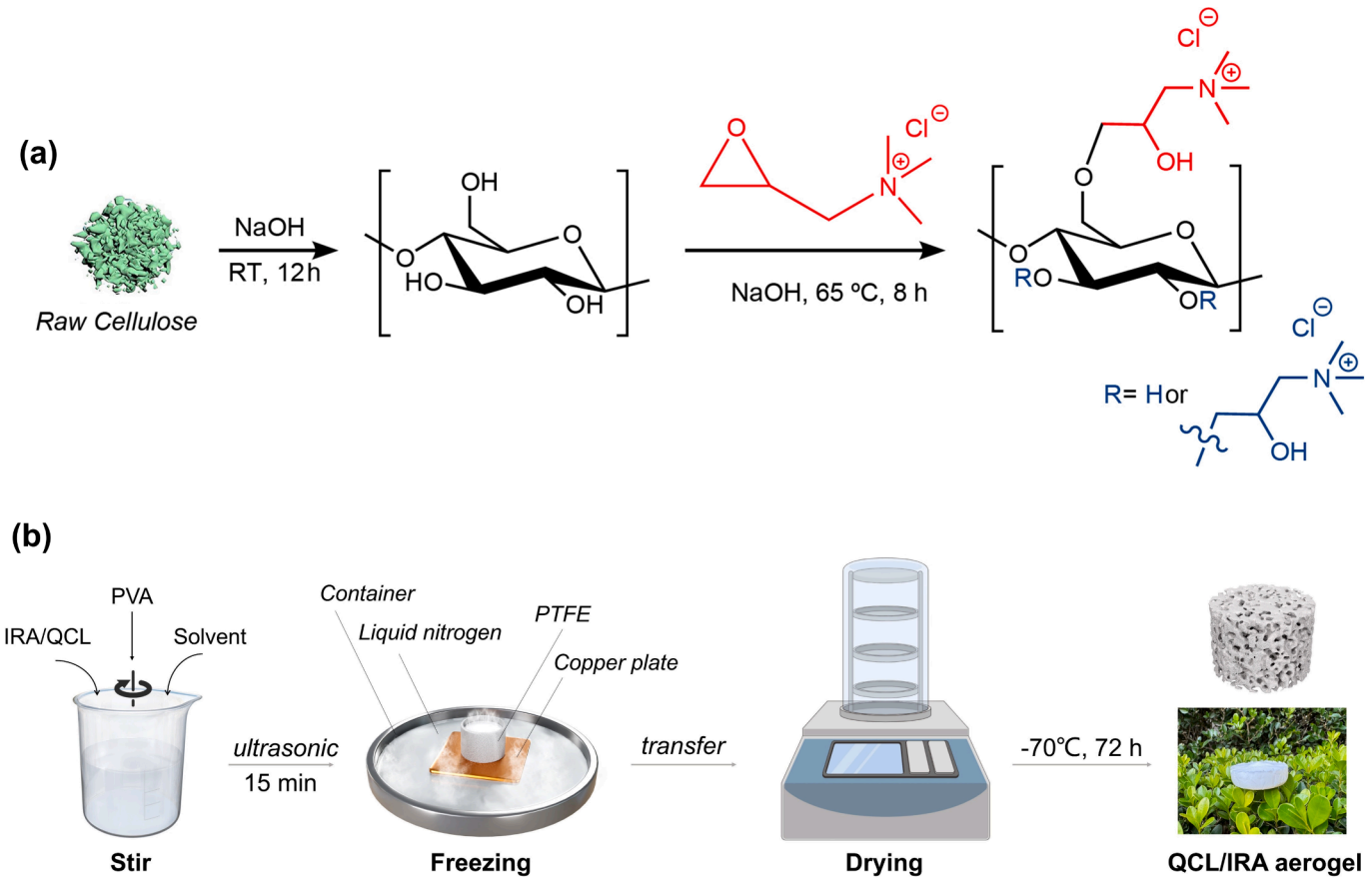

Fig. 1. Schematic of the aerogel adsorbents. (a) Quaternization process of cellulose. (b) Fabrication procedure of the QCL/IRA aerogels.

tested, and the gas leakage error was determined to be neglectable. The CO_2 P/P_0 was maintained at 400 ppm, and the RH in the system was maintained using a laboratory-made humidity control device. The CO_2 and H_2O concentrations were measured using a high-precision gas analyzer (Li-840A). The H_2O concentrations were 5, 10, 15, and 20 parts per thousand (ppt), corresponding to RH values of 21.2 %, 42.3 %, 63.5 %, and 84.7 %, respectively, at 20 ℃. All other specific steps were consistent with those described in our previous study [33].

The CO_2 adsorption capacity q_{ad} (mmol/g) was calculated as follows:

$$q_{ad} = \frac{q_{inj} - c_e V_0 \times 10^{-3}}{m V_m}, \quad (1)$$

where q_{inj} (ml) is the total volume of CO_2 injected into the system, c_e (ppm) is the CO_2 concentration at equilibrium, V_0 (L) is the reactor volume, m (g) is the mass of the resin or cellulose, and V_m (L/mol) is the molar volume.

The CO_2 desorption capacity q_{de} (mmol/g) was calculated as follows:

$$q_{de} = \int_0^{t_{de}} \frac{Q_{N_2} c}{60 \times 10^3 m V_m} dt, \quad (2)$$

where Q_{N2} (L/min) is the N_2 purge flow rate, c (ppm) is the outlet CO_2 concentration, and t_{de} (s) is the desorption time.

To better describe the CO_2 capture conditions in a real adsorption reactor, we defined the CO_2 spatial capture capacity q_m^3 (mol/m^3) using the following expression:

$$q_{m^3} = f \cdot \rho \cdot q_{sa}, \quad (3)$$

where f is the filling rate of the adsorbents in the reactor, ρ is the density of the adsorbent material, and q_{sa} is the CO_2 adsorption capacity of the adsorbent. Because the adsorbents developed in this study can be filled directly into the reactor, f is related to the actual space occupied by the adsorbents inside the reactor; in this work, f was selected as 0.19–0.22.

For the adsorbent adsorption–desorption cycle in the real process, driving the adsorbent adsorption process using continuous purge with 400 ppm CO_2 (air flow) in the adsorption process. The desorption process is driven by spraying water to wet the adsorbent to desorb the CO_2. The desorbed CO_2 can then be further purified by vacuum, distillation and other means of concentration.

2.5. H_2O adsorption and CO_2 adsorption kinetics models

The Guggenheim – Anderson – de Boer (GAB) model, which has been widely used in H_2O sorption studies, was applied to fit the experimental data. The GAB model is expressed as:

$$q_{H_2O} = C_m \frac{C_G K_{ads} h_r}{(1 - K_{ads} h_r)(1 + (C_G - 1) K_{ads} h_r)}, \quad (4)$$

where q_{H2O} is the H_2O adsorption capacity measured in the experiment, C_m (mmol/g) is the H_2O adsorption capacity of the monolayer, C_G and K_{ads} are temperature-dependent parameters, and h_r is the RH.

The pseudo-first-order (PFO), pseudo-second-order (PSO), mixed-order (MO) and Linear models were used to describe the CO_2 adsorption kinetics. The PFO, PSO, and Linear models can be expressed as in **Eq. S1**, **S2** and **S3**, respectively. The MO model is a comprehensive model based on the PFO and PSO models. This model can be written as:

$$q_{ad} = \frac{(q_e k_1 + q_e^2 k_2) e^{-tk_1} - q_e k_1 - q_e^2 k_2}{q_e k_2 e^{-tk_1} - k_1 - q_e k_2}, \quad (5)$$

where q_e is the saturation capacity for CO_2 adsorption, t (min) is the adsorption time, and k_1 and k_2 (min^{-1}) are mixed-order kinetic

constants.

2.6. Quantum chemistry simulations

All quantum chemical simulations were performed using Gaussian 16 based on density functional theory (DFT). B3LYP++G (d, p) was selected as the basis set. For comparison, M062X/def2TZVP and CCSD (T)/cc-pVTZ were also selected as basis sets for parallel calculations. The single-point energy of a specific molecule and the transition state of the reaction between the QA functional group and a CO_2 molecule was simulated. The Mathers hydrophobicity parameter (MHP), which can be written as log $P{\cdot}SA^{-1}$, was calculated to analyze the water vapor hindering ability of the adsorbents [34]. The octanol–H_2O partition constant (log P) of the molecules was calculated using ChemDraw [35]. The surface areas (SA) of the monomer molecules were calculated using Multiwfn [36].

3. Results and discussion

3.1. Optimization of the synthesis of QCL

In our previous study, we confirmed the importance of maintaining the correct alkali-to-cellulose ratio to facilitate quaternization [27]. Excess alkali can impede the quaternization reaction by engaging in side reactions with GTMAC and leach out QA cations, both of which contribute to declines in conversion. Therefore, based on our earlier work, we selected an alkali–CL ratio of 1.2 as the NaOH dosage in this study. We assessed the effects of the reaction time and GTMAC quantity on cellulose quaternization using three variable values based on the literature. To gauge the degree of cellulose quaternization, we introduced the concept of functional group loading (*FGL*), which was calculated as 10 × N%/14, where N% represents the elemental N content measured by elemental analysis [37].

Fig. 2a shows notable differences in the *FGL* values of the different QCL samples. A reaction time of 9 h was insufficient for the quaternization reaction; although *FGL* increased with the GTMAC amount, this reaction time was not as effective as longer reaction times. A reaction time of 18 h appeared to be more suitable, as the *FGL* was maintained at an acceptable level for different amounts of GTMAC. Longer reaction times resulted in minimal gains or even negative effects, possibly because of the conversion of QA cations owing to the prolonged reaction time (for more details, see Table S1). Next, we assessed the quaternization effects of the GTMAC dosage under a reaction time of 18 h (Table 1). A low GTMAC dosage led to an insufficient reaction; that is, excess cellulose remained in the reaction system, leading to low conversion. Conversely, a higher GTMAC dosage led to side reactions. In the FTIR spectra, the characteristic peak of the skeletal vibrations of the QA functional group can be detected at 1428 cm^{-1} [38]. The use of a GTMAC dosage of 8.7 g/g CL resulted in the occurrence of side reactions, as evidenced by the appearance of the typical characteristic peak of primary amine C–N vibrations at 1160 cm^{-1} [39] (Fig. 2b). Thus, considering the reaction conversion rate and time cost, a GTMAC dosage of 5.8 g/g CL and reaction time of 18 h were selected as the optimal synthesis conditions for QCL. The N% of the QCL obtained under these working conditions was 72 % higher than that in our previous work [27].

Table 1
Elemental analysis of cellulose samples with different GTMAC amounts.

	GTMAC dosage	Quaternization time (h)	C (%)	H (%)	N (%)
Raw cellulose	/	/	41.407	6.354	0
Sample 1	2.9 g/g CL	18 h	37.398	6.244	0.895
Sample 2	5.8 g/g CL	18 h	40.696	6.952	1.326
Sample 3	8.7 g/g CL	18 h	39.862	6.644	0.982

3.2. Screening of QCL/IRA aerogels

To facilitate differentiation among the samples, we named the samples according to their type of active component (QCL or IRA) and the weight percentages of these components. For example, the aerogel (Ae) sample Ae-0.5QCL-0.01PVA was prepared with 50 wt% QCL and 1 wt% PVA solution. Aerogel adsorbents were first screened at the pore-structure level. Fig. 3a–d show that all aerogel samples exhibit type-IV N_2 isotherms and type-H3 hysteresis loops, indicating that they have typical mesoporous structures [38]. The pore volume distributions of different pore size ranges indicated that mesopores and macropores were the main components of the pore volume (Fig. 3e). As shown in Table 2, all aerogel samples were dominated by mesopores and macropores, and the average pore size was concentrated in the range of 15–30 nm. This result indicates that the aerogel structure has abundant gas channels for CO_2 mass transfer. The characteristic FTIR spectra of the aerogels are shown in Fig. 3f. PVA exhibits characteristic peaks at 1423 cm^{-1} (bending vibrations of the hydroxyl structure) and 2928 cm^{-1} (asymmetric stretching vibrations of the CH_2 group) [40]. The QA

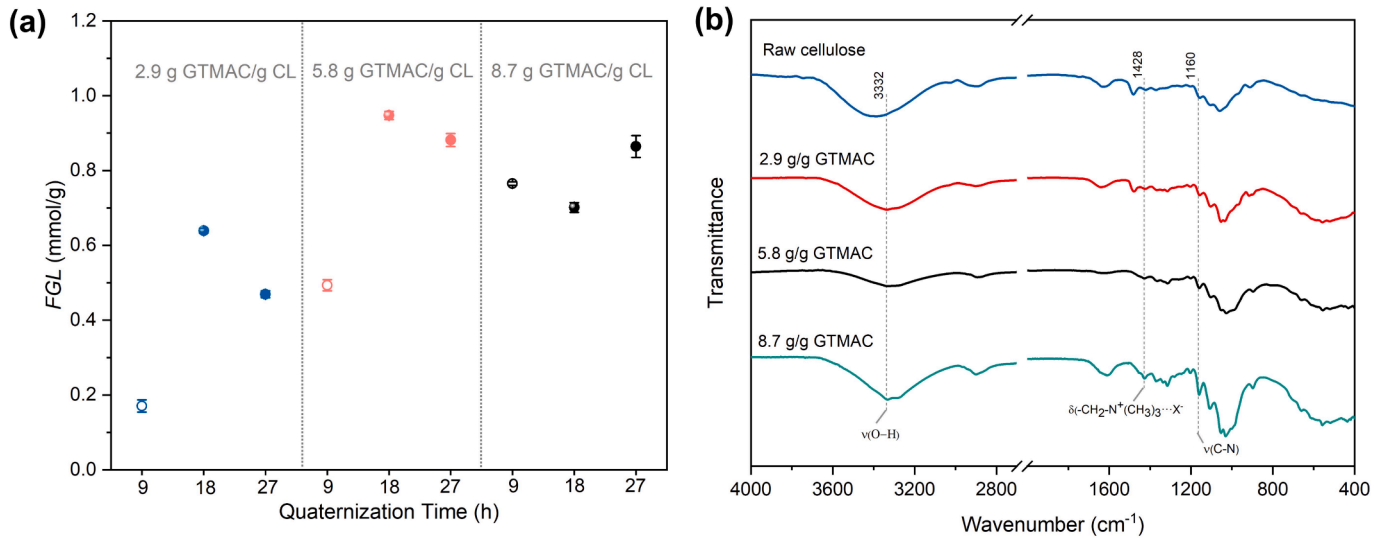

Fig. 2. Quaternization results. (a) Quaternization time and functional group loading (*FGL*). (b) FTIR spectra of raw cellulose and QCL.

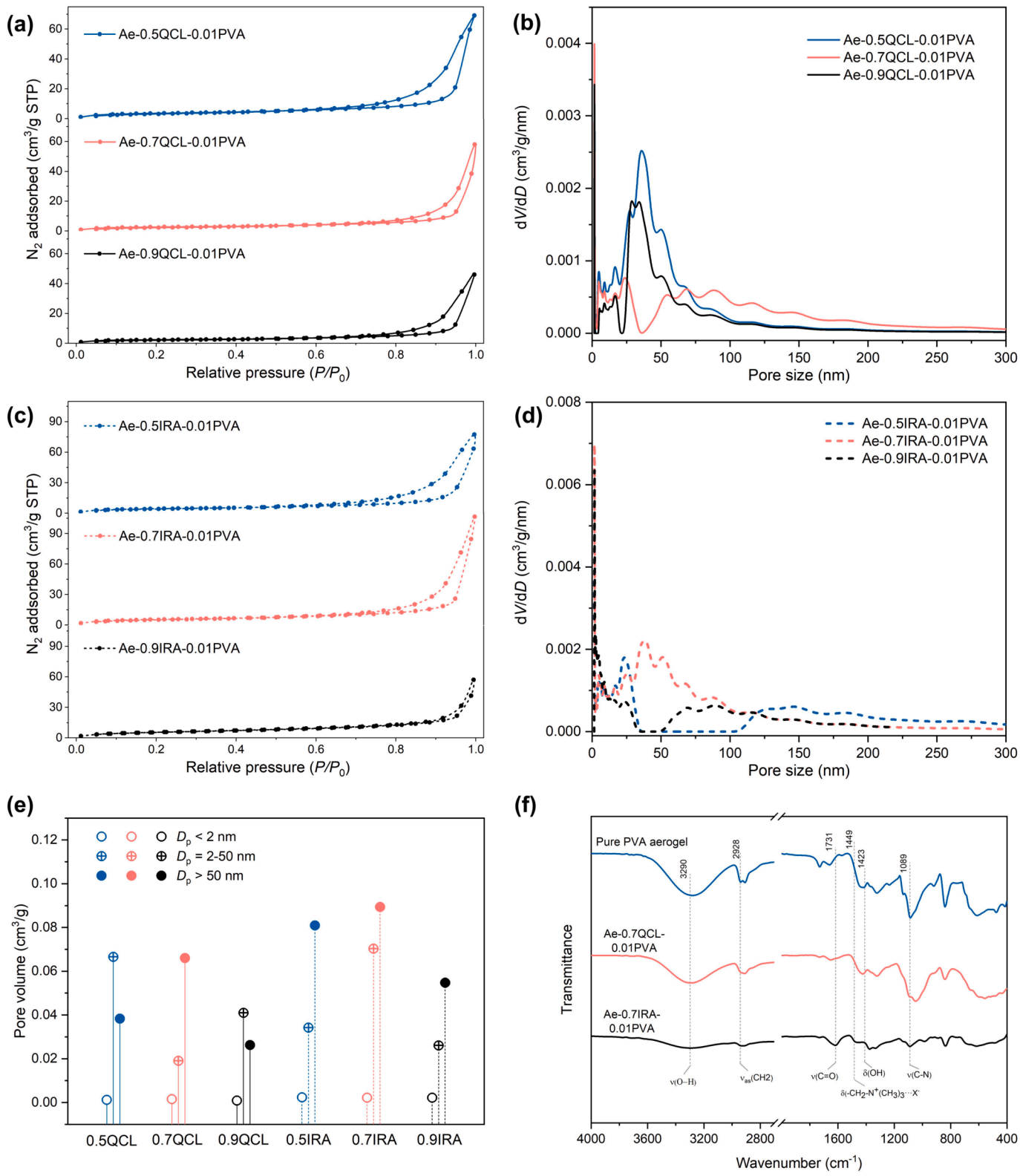

Fig. 3. Pore structure characterization. (a) N_2 physisorption isotherms of the QCL aerogels. (b) Pore size distributions of the QCL aerogels calculated using the NLDFT model. (c) N_2 physisorption isotherms of the IRA aerogels. (d) Pore size distributions of the IRA aerogels calculated using the NLDFT model. (e) Pore volumes of QCL and IRA aerogels with different pore size ranges. (f) FTIR spectra of the aerogels.

functional group exhibits characteristic peaks at 1449 cm^{-1} (skeletal vibrations), 1089 cm^{-1} (C-N stretching), and 1728 cm^{-1} (C=O stretching) [33], indicating that the active functional group was not modified or detached during the fabrication of the aerogel adsorbents.

The BET surface area and pore volume the QCL aerogels decreased with increasing QCL dosage because PVA, when prepared into an aerogel, tends to become more porous than cellulose, which has pores at the micrometer level and lacks inherent pores. Consequently, the pore

Table 2
BET surface areas, pore volumes, and pore diameters of all aerogel samples.

	S_{BET} (m^2/g)	Pore volume (cm^3/g)	Nonmicropore pore volume (cm^3/g)	Average pore diameter (nm)
Ae-0.5QCL-0.01PVA	14.37	0.106	0.105	21.76
Ae-0.7QCL-0.01PVA	10.72	0.087	0.085	29.85
Ae-0.9QCL-0.01PVA	9.84	0.068	0.067	24.71
Ae-0.5IRA-0.01PVA	17.43	0.117	0.115	19.71
Ae-0.7IRA-0.01PVA	20.75	0.162	0.160	26.17
Ae-0.9IRA-0.01PVA	20.47	0.083	0.081	16.27

structures of QCL aerogels prepared with higher QCL dosages were nonideal for their intended purpose. By contrast, the IRA aerogels showed improved BET SA and pore volumes compared with the QCL aerogels at different IRA dosages owing to the abundant pores present in the IRA powder. However, aerogels prepared with higher IRA dosages are easily loosened and exhibit poor mechanical strength. Therefore, from the perspective of pore structure, moderate dosages of both QCL and IRA are recommended. In summary, aerogel materials produced through the freezing–ice-templating method demonstrated significant improvements in pore space compared with the earlier adsorbents QAR-CA [33]. The enriched pore structure of the aerogels prepared in this work plays a crucial role in enhancing CO_2 mass transfer and accelerating the CO_2 adsorption process.

The unidirectional freezing–ice-templating method plays a significant role in the creation of numerous laminar pores, as depicted in the SEM images of the aerogel adsorbents in Fig. 4. The overviews of the QCL and IRA aerogels revealed CL fibers blended with PVA, creating a virtually indistinguishable mixture. The IRA powder was enclosed within the laminar structure of the PVA. Notably, aerogels with different dosages of the active component exhibited variations in pore structure. For the QCL aerogels, a distinct layer-like aerogel structure with evenly distributed pores within and between layers was observed; this structure is a characteristic of materials prepared using the freezing–ice-templating method [41]. The EDS profiles of the IRA aerogels revealed a uniform IRA powder distribution (Fig. S3). The IRA aerogels exhibited a heterogeneous structure. Aerogels prepared with 50 and 70 wt% IRA showed a hierarchical structure, while that prepared with 90 wt% IRA revealed no regularity. Differences in plasticity between IRA powder and QCL could result in a pore structure that may contain dead pores in the IRA aerogels, which would impede gas-phase mass transfer. By contrast, CO_2 transport within the pores of the QCL aerogels may occur smoothly.

After the initial screening of the aerogel adsorbents based on their pore structure, their CO_2 capture performance was screened using CO_2 adsorption tests. The same RH (21.2 % RH) was maintained in all tests, and the CO_2 concentration was maintained at 400 ppm to assess the adsorption performance of the materials at ultralow CO_2 concentrations; the CO_2 $t_{1/2}$ was used as the kinetic index for material evaluation. The CO_2 adsorption capacity of the QCL aerogels increased with increasing QCL dosage, and $t_{1/2}$ was slowest at 90 wt% QCL, which could be attributed to the poor pore structure and slow gas-phase mass transfer rate of the material resulting from high QCL dosage used (Fig. 5a). Both the CO_2 adsorption capacity and $t_{1/2}$ of the IRA aerogels showed optimal values at a 70 wt% dosage. However, all IRA aerogel adsorbents exhibited low CO_2 adsorption performance (Fig. 5b).

3.3. Optimization of the pore structure of the IRA aerogel adsorbents

In the preceding section, we observed the absence of a regular interlayer pore structure in the IRA aerogels, which raises concerns on the potential presence of dead or poorly connected pores that could impede CO_2 gas-phase mass transfer. Thus, we sought to enhance the pore structure of the IRA aerogels. As shown in Fig. 4, the interlayer pore spacing of the PVA-containing aerogels is only a few micrometers. Our attempt to effectively encapsulate IRA powder with a particle size of 75 μm within these interlayer pores proved to be challenging, leading to the unfortunate loss of active components. Owing to the robust plastic toughness of the resin particles, conventional ball milling was ineffective in further reducing the particle size. Thus, we employed mechanical pulverization to control the IRA powder particle size to 50 and 40 μm. Adjustments to the concentration of the PVA solution also played a crucial role in optimizing the dispersion of the IRA powder within the solution by preventing powder settling.

Fig. 6a shows the apparent morphology of Ae-0.7IRA (40 μm)-0.01PVA. The predominant feature along the longitudinal axis of the aerogel was the encapsulation of the IRA powder within the PVA lamellar structures. A more regular lamellar pore structure can be observed in the radial direction. Smaller particle sizes facilitated better integration of the IRA powder into the PVA lamellar structure, simultaneously serving as pore expanders and increasing the interlayer pore spacing from a few micrometers to 10 μm or larger. The pore structure appeared as a cross-structure comprising monolayer active components and nanoscale layered carriers. Larger particle sizes (75 μm) are correlated with increased density, leading to the settling of the IRA powder in

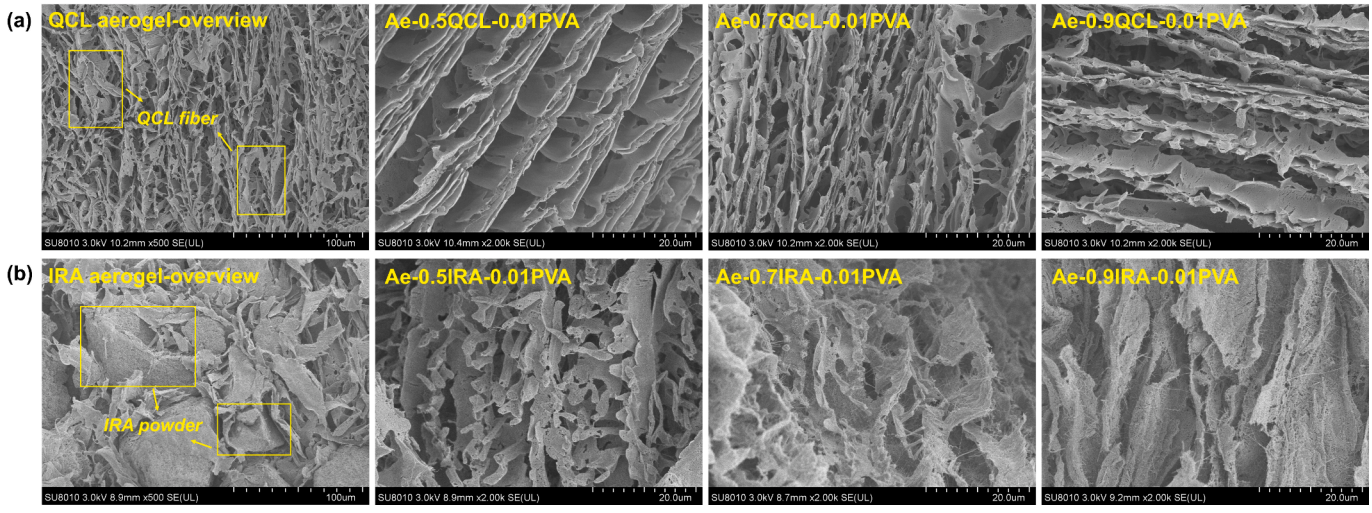

Fig. 4. SEM images of the (a) QCL and (b) IRA aerogels.

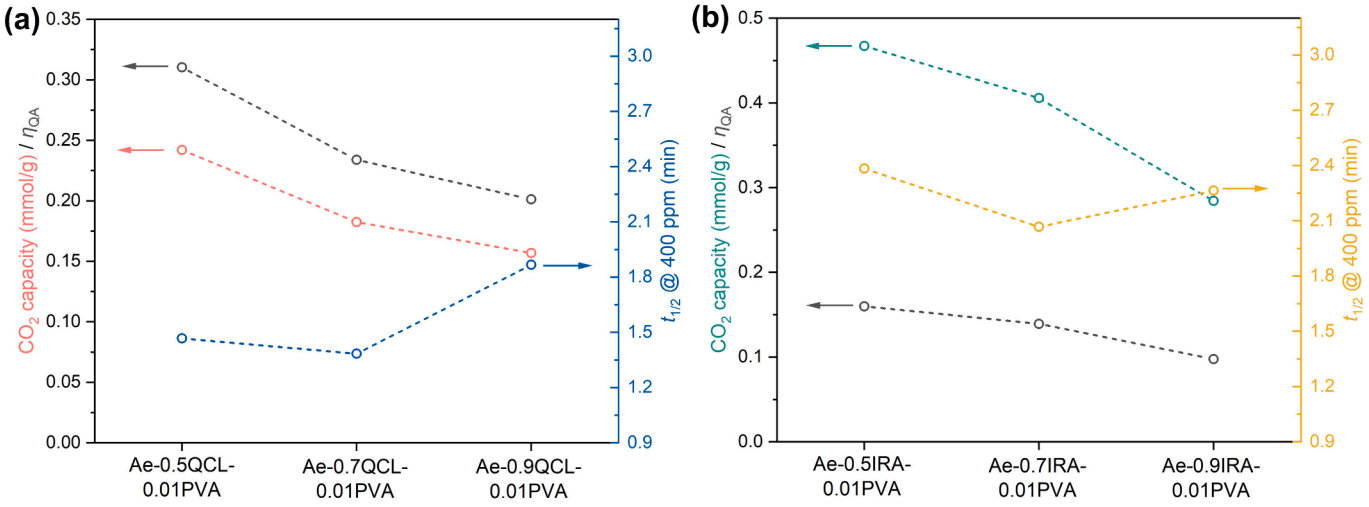

Fig. 5. CO_2 adsorption capacity, $t_{1/2}$, and η_{QA} at 400 ppm and 21.2 % RH of the (a) QCL and (b) IRA aerogels.

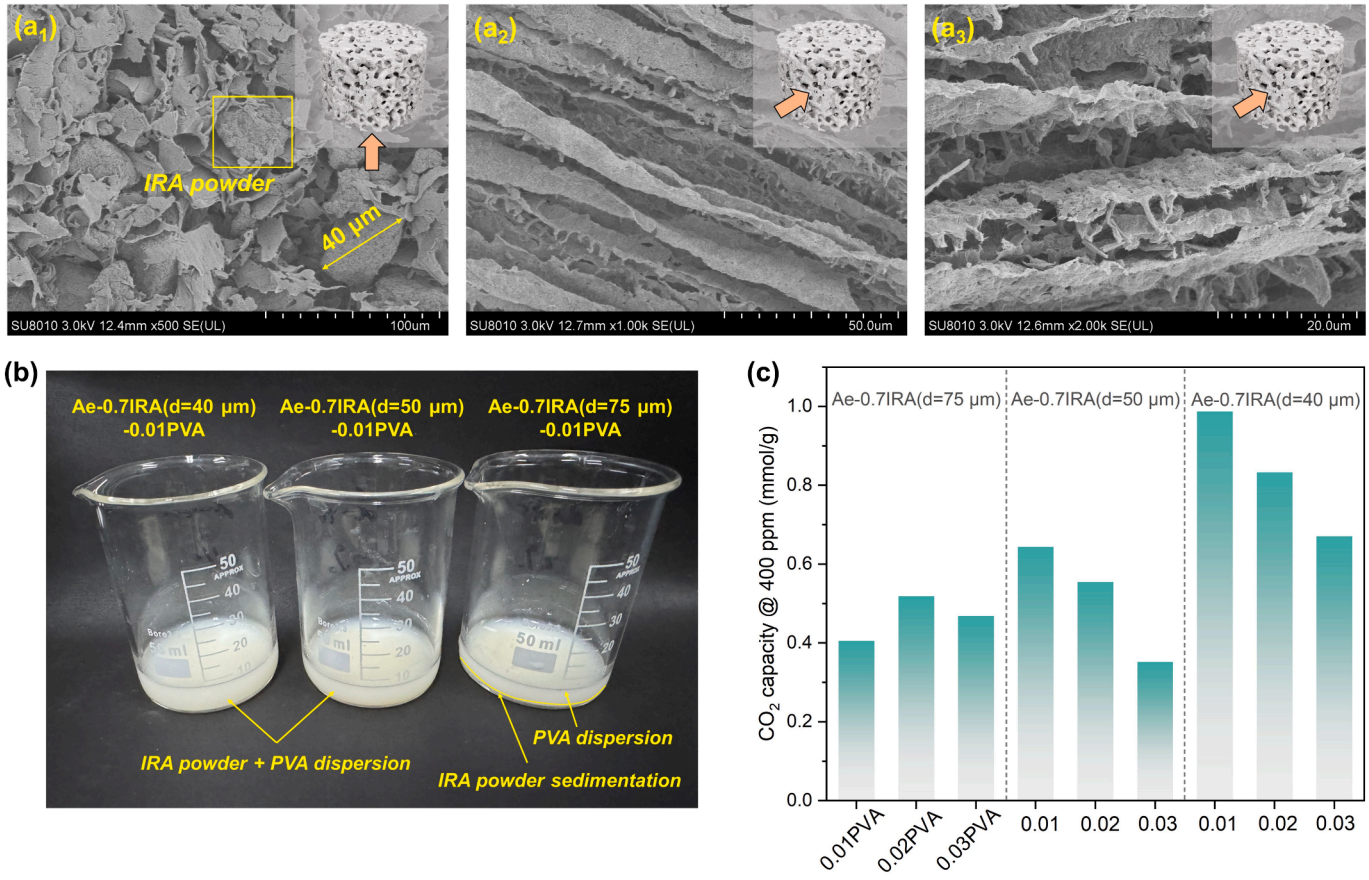

Fig. 6. Optimization results of the IRA aerogel adsorbents. (a) SEM images of Ae-0.7IRA (d=40 μm)-0.01PVA. (b) Photograph of the IRA aerogel dispersion. (c) CO_2 adsorption capacity at 400 ppm and 21.2 % RH of aerogels with different IRA powder sizes and PVA concentrations.

the PVA solution (Fig. 6b and Table S2). Smaller particle sizes enabled the uniform dispersion of the IRA powder in the PVA solution and prevented pore discontinuities caused by powder buildup, which would otherwise impede gas-phase mass transfer (Fig. S4). According to the pore structural parameters detailed in Table 3, Ae-0.7IRA (40 μm)-0.01PVA exhibits the highest pore volume among the IRA aerogels. The CO_2 adsorption capacity of this aerogel aligned with the optimization of its pore structure (Fig. 6c). Specifically, Ae-0.7IRA (40 μm)-0.01PVA demonstrated a CO_2 capacity of 0.99 mmol/g at 20 °C and 21.2 % RH.

Interestingly, reducing the particle size of the resin powder actually decreased the specific surface area of the aerogels. The specific surface area originates from both the pores within the resin particles and those formed in the resin–PVA connections. The use of smaller particles facilitates greater exposure of the resin particles, incorporating the pores within the resin into the specific surface area measurements. Consequently, the overall specific surface area of the aerogel decreased owing to the smaller specific surface area of the resin particles, as evidenced by the SEM images illustrating the effective exposure of the resin particles

Table 3
BET surface areas, pore volumes, and pore diameters of the IRA aerogel adsorbents.

IRA aerogel	S_{BET} (m^2/g)	Pore volume (cm^3/g)	Average pore diameter (nm)
Ae-0.7IRA (d = 75 μm)-0.01PVA	20.75	0.162	26.17
Ae-0.7IRA (d = 75 μm)-0.02PVA	30.69	0.161	21.21
Ae-0.7IRA (d = 75 μm)-0.03PVA	32.71	0.152	23.08
Ae-0.7IRA (d = 50 μm)-0.01PVA	29.49	0.204	29.78
Ae-0.7IRA (d = 50 μm)-0.02PVA	31.15	0.174	23.22
Ae-0.7IRA (d = 50 μm)-0.03PVA	32.33	0.148	23.90
Ae-0.7IRA (d = 40 μm)-0.01PVA	19.18	0.227	33.08
Ae-0.7IRA (d = 40 μm)-0.02PVA	18.32	0.210	34.97
Ae-0.7IRA (d = 40 μm)-0.03PVA	18.27	0.184	35.70

(Fig. S4). Therefore, the freezing–ice-templating method is instrumental in generating a higher number of active resin particles within the same aerogel mass, thereby enhancing the exposure of the resin particles previously encapsulated in PVA and contributing to a better pore structure. The unique micro/mesoporous composite structure of the adsorbents is conducive to gas-phase transport. Overall, given their excellent pore structure and good CO_2 capture performance, Ae-0.7QCL-0.01PVA and Ae-0.7IRA (d=40 μm)-0.01PVA were selected as high-quality aerogel adsorbents, and their moisture swing adsorption/desorption performance was further investigated.

3.4. CO_2 capture performance of the high-quality aerogels

The regularity of the CO_2 capture performance of the high-quality aerogel adsorbents for moisture swing was tested (Fig. 7a-b). The CO_2 adsorption performance of the aerogel adsorbents varied with the moisture swing over a wide range of RHs (Table S3). Interestingly, unlike previous moisture swing adsorbents, we found that the CO_2 adsorption capacity of both Ae-0.7QCL-0.01PVA and Ae-0.7IRA (d=40 μm)-0.01PVA tended to increase and then decrease with the change in RH. Under the experimental conditions adopted in this study, both adsorbents achieved maximum CO_2 adsorption capacities at 63.5 % RH.

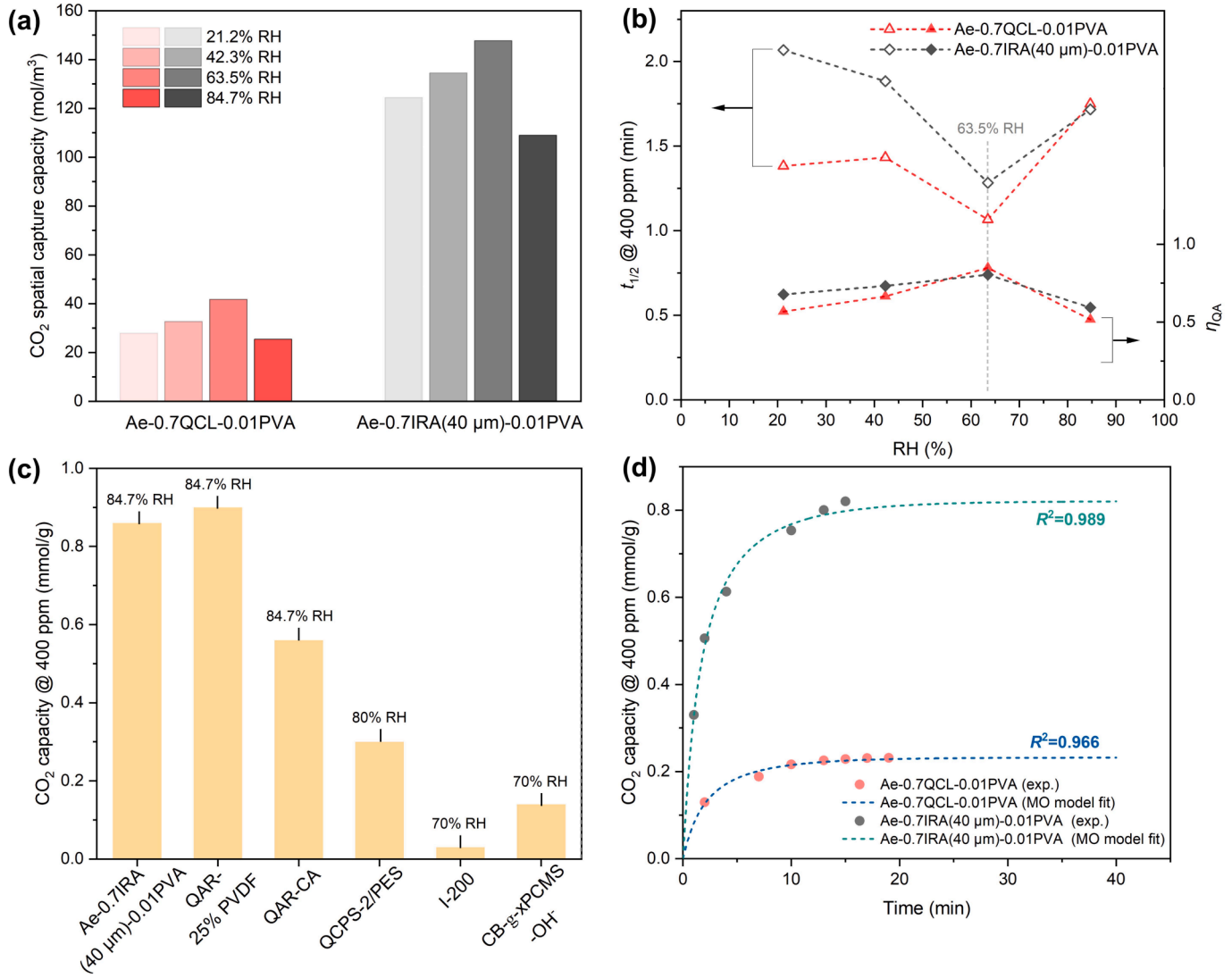

Fig. 7. Comparison of the CO_2 capture performance of Ae-0.7QCL-0.01PVA and Ae-0.7IRA (d=40 μm)-0.01PVA. (a) CO_2 adsorption capacity at different relative humidities (RHs). (b) $t_{1/2}$ and η_{QA} at different RHs. (c) CO_2 adsorption capacity at high RH. (d) Kinetic model fitting.

The performance of adsorbents under sub-ambient conditions should also be of concern [10]. Then, we tested the CO_2 adsorption performance of adsorbents at higher and lower temperature/humidity conditions (Fig. S5). Temperature mainly affected the CO_2 adsorption rate, and sub-ambient temperatures caused ice to clog partial pores of the adsorbent, resulting in attenuation of CO_2 adsorption capacity and rate. The adsorbent maintained high CO_2 adsorption capacity over a wide range of humidity (<80 % RH), and higher relative humidity exacerbated the competing adsorption of water vapor, affecting the adsorption reaction equilibrium.

Functional group efficiency was defined as $\eta_{QA}=q_{CO2}/q_N$, where q_{CO2} is the CO_2 adsorption capacity of an adsorbent at a specific humidity level (measured at 20 °C and CO_2 P/P_0 of 40 Pa). The η_{QA} of Ae-0.7QCL-0.01PVA was 0.52–0.85, while that of Ae-0.7IRA (d=40 μm)-0.01PVA was 0.59–0.80. When η_{QA} was increased by 5.8 times, the IRA adsorbent demonstrated excellent CO_2 q_{m3} (148 mol/m^3) and a short $t_{1/2}$ (1.28 min). However, a high q_{m3} value is not always optimal. The negative effects of high filling rates or material densities on adsorbent-filled devices such as zeolites [42], silica [43,44], and MOFs [45] have been reported in previous simulation studies. Excessive filling rates lead to a sharp increase in pressure drop and significant energy consumption. A high material density indicates a lack of porosity, leading to poor CO_2 adsorption kinetics and reductions in the operating efficiency of the device. Ae-0.7IRA (d=40 μm)-0.01PVA is a suitable choice as an adsorbent because it exhibits both excellent q_{m3} and kinetics. Even at a high RH, Ae-0.7IRA (d=40 μm)-0.01PVA exhibited high CO_2 adsorption capacity compared with other moisture swing adsorbents [33,38,46] (Fig. 7c).

The CO_2 adsorption rates of the two aerogel adsorbents were analyzed at different humidity levels. The adsorption behavior of the aerogels was first fitted using three adsorption kinetic models (Fig. 7d and Fig. S6), namely, the PFO [47], PSO [48], MO [6] and Linear [49] models, and the corresponding fitting parameters and R^2 are given in Table 4 and Table S4. Among the three models, the MO model showed the best fit, followed by the PSO and PFO models, likely because the PSO model is more suitable for describing chemical adsorption while the PFO model is more suitable for describing physisorption. The MO model combines the features of both the PSO and PFO models, and yielded results that were more consistent with the CO_2 adsorption procedure at 400 ppm. We believe that the adsorption process at ultralow CO_2 concentrations is characterized by weak chemical interactions; thus, the MO model best describes the CO_2 adsorption process of the adsorbents in this study. Fig. S7 shows the dimensionless CO_2 adsorption rate, which varies with the adsorption saturation. Compared with the QAR-CA adsorbent prepared in a previous study, the high-quality aerogel adsorbents synthesized in this study had better CO_2 adsorption rates, thus reflecting the advantages of the freezing–ice-templating method for forming excellent pore structures [33]. If using continuous purge with 400 ppm CO_2 (air flow) in the real process, the adsorbent required ~ 30 min to reach 90 % adsorption saturation (Fig. S8).

Moisture swing adsorbents usually exhibit high sensitivity to humidity changes, which restricts their applications [25]. These adsorbents typically perform well at RH values below 30 %; however, real-world environments often maintain moderate levels of humidity (50 %–60 % RH). The CO_2 adsorption capacity of the high-quality aerogel adsorbents initially increased and then decreased in response to changes in RH. This behavior differs from that of conventional moisture swing adsorbents. PVA with high alcoholysis degree (99 %) had poor water solubility, because the intermolecular hydrogen bonding strength of PVA with high alcoholysis degree increased, preventing the formation of hydrogen bonds between PVA and water molecules. We hypothesized that the water vapor hindering ability of the aerogels (compared with that of conventional adsorbents) caused this difference. The results of the H_2O vapor adsorption tests and static H_2O contact angles of our aerogels support our viewpoint. Fig. 8a shows the difference in H_2O vapor adsorption at different RHs, which were fitted using the GAB model. A substrate-free pure PVA aerogel was used for comparison. Compared with this aerogel, Ae-0.7IRA (d=40 μm)-0.01PVA had higher H_2O vapor adsorption whereas Ae-0.7QCL-0.01PVA had slightly lower H_2O adsorption, indicating their hydrophilicity at the macroscopic level. The pure PVA aerogel exhibited an overall lower H_2O adsorption capacity, indicating its water vapor hindering ability. The GAB model assumes the occurrence of multilayered adsorption, and the fitting parameters obtained reflect the monolayer H_2O adsorption of each aerogel (see C_m in Table S5). C_m is more indicative of the difference in the hydrophilicity of the materials than the macroscopic H_2O vapor adsorption results. The monolayer adsorption of H_2O by Ae-0.7IRA (d=40 μm)-0.01PVA was 3.327 mmol/g, which reflects strong hydrophilicity. This result agrees with the results of the macro-level experiment and is corroborated by the results of the static H_2O contact angle tests (Fig. 8c).

Although the high-quality aerogel adsorbent generally exhibited macroscopic hydrophilicity, the addition of PVA increased its water vapor hindering ability. This enhancement resulted in a backward shift in their CO_2 adsorption peak against changes in humidity. The H_2O and CO_2 adsorption rates of Ae-0.7QCL-0.01PVA and Ae-0.7IRA (d=40 μm)-0.01PVA were compared from the perspective of kinetics, as shown in Fig. 8b and Table 5. Fig. 8b shows that CO_2 adsorption by the adsorbents reaches completion within approximately 0.4 h, while H_2O adsorption reaches completion after nearly 6 h. This observation indicates the high selectivity of the aerogel adsorbents for CO_2. The dashed line in Fig. 8b indicates that dynamic equilibrium is maintained after reaching CO_2 adsorption saturation, and only the H_2O adsorption process continues. Using the dimensionless adsorption rates at the same CO_2 (θ) and H_2O (θ') adsorption saturation, we can analyze the difference in adsorption rates even if the same level of saturation is not reached at the same time. When θ and θ' are 0.6, both Ae-0.7QCL-0.01PVA and Ae-0.7IRA (d=40 μm)-0.01PVA have CO_2 adsorption rates that were approximately six times higher than their H_2O adsorption rates. As saturation increased, the gap between the two rates widened by an order of magnitude, indicating faster CO_2 adsorption. Although the H_2O adsorption rate of the pure PVA aerogel is lower than that of the QCL/IRA aerogel, the difference is not substantial. This finding suggests that the QCL/IRA aerogels have improved the water vapor hindering ability compared with the substrate alone because of the presence of PVA as the skeleton support material for the aerogel. This enhancement leads to variations in the H_2O/CO_2 adsorption rates and adsorption selectivity of the prepared aerogels.

The moisture swing regeneration procedure for the aerogel adsorbents was driven by 100 % RH moisture–N_2 purging under 20 °C. Although the water vapor hindering ability of the aerogel adsorbents was high, they retained their moisture swing regeneration properties. In fact, both adsorbents only demonstrated a change in their peak CO_2 adsorption capacity (at 63.5 % RH), and this peak did not affect the decrease in their adsorption capacity at higher humidity (e.g., at 84.7 % RH). Thus, they can still achieve low-energy CO_2 regeneration via moisture swing. The differences between the two aerogel adsorbents during CO_2 desorption are shown in Fig. 9a. Ae-0.7IRA (d=40 μm)-0.01PVA had higher CO_2 desorption capacity (0.52 mmol/g) and a faster desorption rate (~11.5 min to reach equilibrium) than Ae-0.7QCL-0.01PVA (at 0.24 mmol/g and ~ 31 min, respectively). The difference in the CO_2 desorption capacity of these adsorbents is due to differences in their CO_2 adsorption capacity. Although the higher adsorption capacity of Ae-0.7IRA (d=40 μm)-0.01PVA leads to increased desorption,

Table 4
Kinetic parameters of the MO model for the high-quality aerogels.

	Adsorption condition	MO model fit		
		k_1	k_2	R^2
Ae-0.7QCL-0.01PVA	400 ppm, 20℃, 63.5 % RH	0.163	1.475	0.966
Ae-0.7IRA (d = 40 μm)-0.01PVA		0.149	0.589	0.989

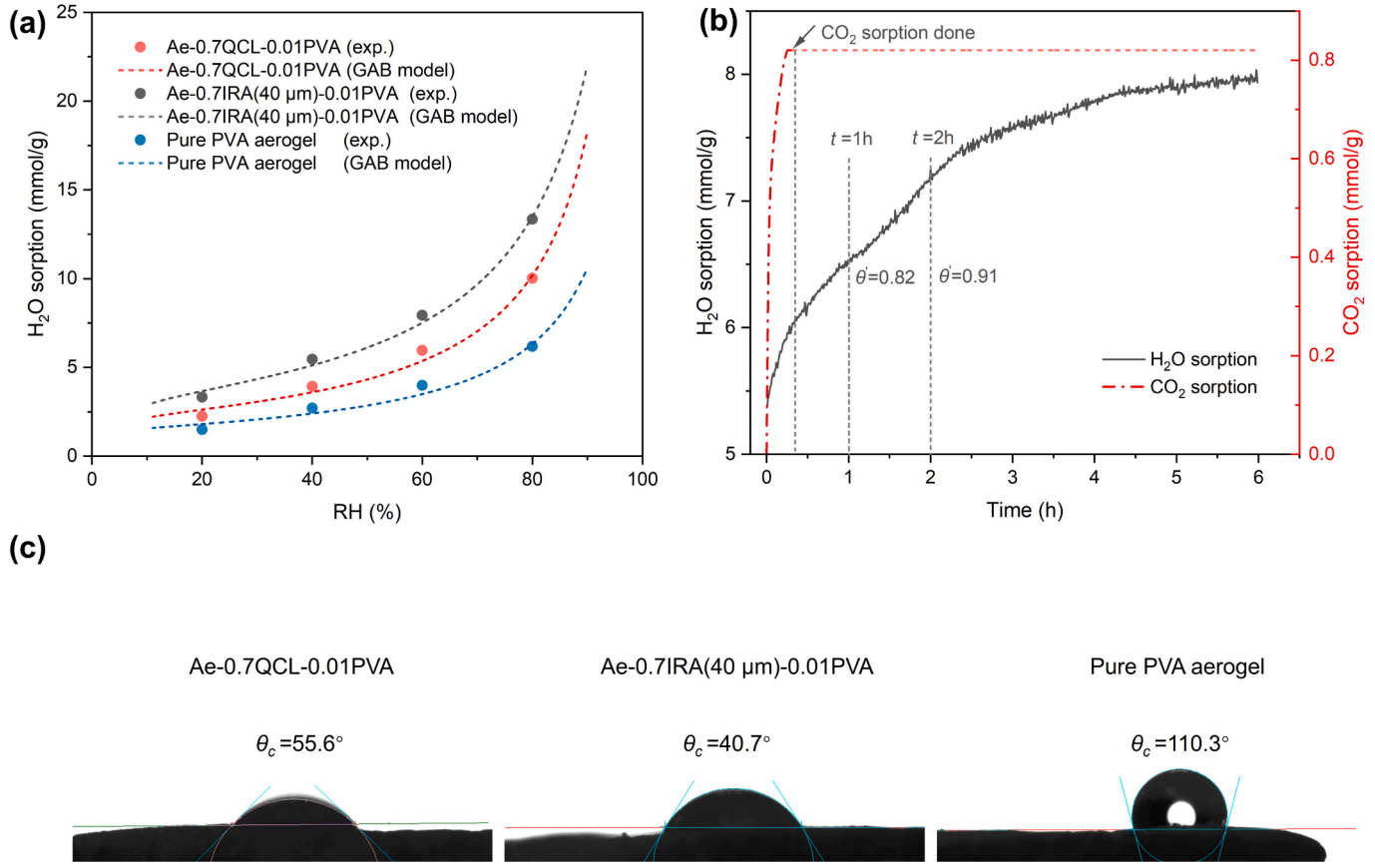

Fig. 8. Water vapor characterization of aerogel adsorbents. (a) H_2O adsorption capacity and GAB model fitting of the QCL/IRA aerogels. (b) H_2O/CO_2 adsorption kinetics of Ae-0.7IRA (d=40 μm)-0.01PVA at 20 ℃ and 63.5 % RH. (c) Static H_2O contact angles of the QCL, IRA, and pure PVA aerogels.

Table 5
Comparison of the H_2O/CO_2 adsorption rates of different aerogels.

	Conditions	Saturation	H_2O adsorption rate (1/s)	CO_2 adsorption rate (1/s)
Ae-0.7QCL-0.01PVA	400 ppm, 20 °C 63.5 % RH	θ, θ'=0.6	1.3×10^{-3}	7.8×10^{-3}
		θ, θ'=0.8	4.5×10^{-4}	4.1×10^{-3}
		θ, θ'=0.9	1.5×10^{-4}	2.8×10^{-3}
Ae-0.7IRA (d = 40 μm)-0.01PVA		θ, θ'=0.6	1.1×10^{-3}	6.6×10^{-3}
		θ, θ'=0.8	3.1×10^{-4}	5.0×10^{-3}
		θ, θ'=0.9	1.3×10^{-4}	3.6×10^{-3}
Pure PVA aerogel		θ'=0.6	1.0×10^{-3}	/
		θ'=0.8	2.7×10^{-4}	/
		θ'=0.9	1.3×10^{-4}	/

its desorption ratio (q_{de}/q_{ad}) is also high. Specifically, the discrepancy in the desorption ratio directly influences the desorption rate. Overall, the desorption times of the two high-quality aerogel adsorbents were faster than those reported in previous studies. In addition, the ability of these adsorbents to retain their moisture swing regeneration property enabled them to capture and regenerate CO_2 in a highly kinetic (either adsorption or desorption) form without requiring high energy consumption. There was no temperature change in the regeneration process, the regeneration energy consumption was approximately equal to the heat of adsorption. The CO_2 adsorption heat of the adsorbent at 20 ℃ and 60 % RH was 25.69 KJ/mol (Fig. S9). This value was affected by the ambient humidity, presenting an interesting phenomenon of spontaneous cooling absorption [50].

Considering the reusability of this adsorbent, the working capacity of Ae-0.7IRA (d=40 μm)-0.01PVA was tested in a cycle at 400 ppm, 20 ℃, as shown in Fig. 9b. The results showed that no obvious decrease of CO_2 saturation capacity was found in 20 times tests, which meant the cycling stability. The adsorbent did not degrade under high humidity conditions. The degree of regeneration (q_i/q_{1st}) was above 90 % in all 10 cycles, indicating that the adsorbent was almost fully regenerated. The cyclic capacity of shaped adsorbent was ~ 0.52 mmol/g. Meanwhile, the adsorbent was supplemented with a 180-day long-term adsorbent degradation tests at ambient temperature (Fig. S10). The results showed that the capacity of the adsorbent only decreased by ~ 4 % after 180 days at ambient conditions, which reflected its good stability. Since cross-linked polystyrene is basically very stable, the quaternary ammonium modification product has significantly better anti-degradation performance than its cellulose-based counterpart. The major challenge facing the amine adsorbents is the severe oxidative degradation during regeneration at high temperatures, while the quaternary ammonium polymers have a clear advantage in terms of long-term operational stability.

3.5. Calculation of water vapor hindering parameters

In Section 3.4, the hydrophilicity of the aerogel adsorbents was described thermodynamically and kinetically through H_2O vapor adsorption tests and static H_2O contact angle tests; however, these analyses are limited to the macroscopic level. In this section, a description of water vapor hindering ability at the microscopic level and the hypothetical mechanism of the H_2O effect on the adsorbents upon reaching peak adsorption capacity at medium RH are provided (Fig. 10). First, we examined the water vapor hindering ability of three bases, namely, PS, CL, and PVA; the first two bases do not carry QA functional groups because QA cations are strongly hydrophilic. Surface area cloud plots of the three bases are shown in Fig. S11. The MHP values used to quantify the water vapor hindering ability of the materials are given in Fig. 10a,

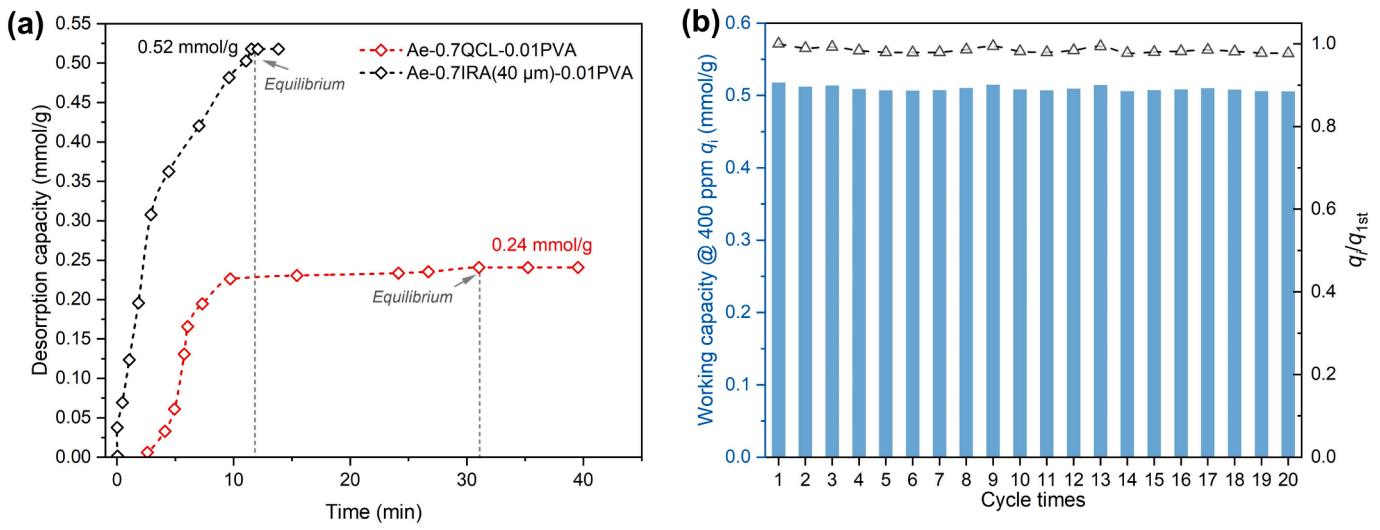

Fig. 9. The aerogel adsorbents assessment. (a) Desorption capacity of the QCL or IRA aerogel adsorbents at 100% RH. (b) The working capacity of IRA aerogel adsorbent during 20 consecutive cycles.

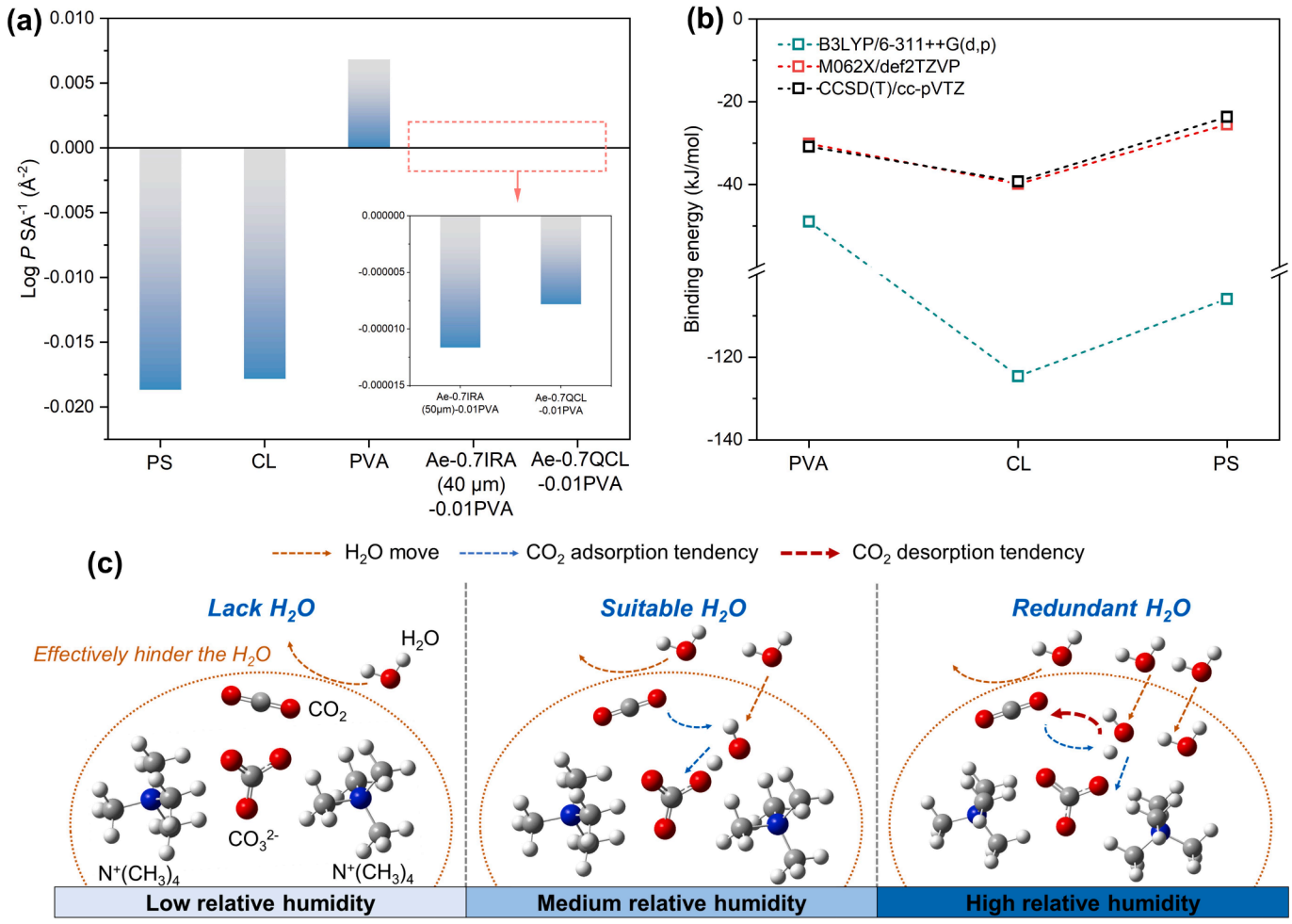

Fig. 10. Molecular scale calculations results. (a) MHP values. (b) Binding energies of different bases. (c) Transition-state calculations at different RH conditions.

with PVA showing stronger water hindering ability than PS and CL. PS was more hydrophilic than CL. The water vapor hindering ability of these bases was significantly improved when prepared as aerogel adsorbents, as depicted in the embedded plots in Fig. 10a. The differences in the binding energies of the three bases with respect to H_2O are shown in Fig. 10b. The binding energies were calculated using Gaussian with three different sets of computational bases [51]. The B3LYP/6-311++G (d, p) basis set is not informative because of its low computational

accuracy, and the difference between the calculated results of the two other basis sets reflected higher accuracy. Taking the results of the CCSD (T)/cc-pVTZ basis group as an example, the binding energies of the three bases did not differ significantly; however, the hydrophilicity of the QA cation led to the aerogel adsorbent exhibiting stronger hydrophilicity than the pure PVA aerogel, which was consistent with our macro-level analysis.

To better analyze the effect of H_2O on CO_2 adsorption, we represented low, medium, and high RHs by simulating different numbers of H_2O molecules. The reaction equation for CO_2 adsorption is as follows [52]:

$$CO_3^{2-} + H_2O + CO_2 \rightarrow 2HCO_3^- \quad (6)$$

For QA cations with CO_3^{2-} as the counter anion, H_2O is necessary for CO_2 adsorption [50]. Fig. 10c shows the transition states of the reaction for different numbers of H_2O molecules, corresponding to different RH conditions. The CO_2 active adsorption sites of the aerogel adsorbents had poor access to the H_2O molecules at low RH, resulting in a lag or cessation of CO_2 adsorption. As the RH increased, however, the number of accessible H_2O molecules increased and the CO_2 adsorption capacity of the adsorbents increased. When the RH was further increased, the presence of redundant H_2O hindered the continuation of the CO_2 adsorption, causing the reaction equilibrium to move toward the direction of desorption, and the CO_2 adsorption capacity of the adsorbents decreased. This mechanism of the H_2O effect at high humidity is similar to that observed in previous resin adsorbents, thus supporting the idea that the aerogel adsorbents have moisture swing regeneration ability. The change in activation energy also confirmed the mechanism of the H_2O effect (Fig. S12).

4. Conclusion

In summary, a method based on unidirectional freezing–ice-templating was proposed to fabricate aerogel adsorbents oriented toward moisture swing adsorbents. The synthesized aerogel adsorbents exhibited ultrahigh CO_2 adsorption kinetics. Two substrate materials, QCL and IRA, were used to prepare the aerogel adsorbents. A GTMAC dosage of 5.8 g/g CL and reaction time of 18 h were found to be optimal conditions for cellulose quaternization. The optimal amounts of the substrates for aerogel adsorbent preparation were screened via pore structure and CO_2 adsorption capacity analyses. The pore structure of the IRA aerogel adsorbents was optimized by controlling the powder size and PVA concentration. Interestingly, the CO_2 adsorption capacity of the two best-quality aerogel adsorbents, Ae-0.7QCL-0.01PVA and Ae-0.7IRA (d=40 μm)-0.01PVA, tended to first increase and then decrease in response to RH changes, with their adsorption capacity peaking at ~ 60 % RH. The macroscopic tests and microscopic simulations revealed an interesting phenomenon. At the macroscopic level, both H_2O vapor adsorption and static H_2O contact angle tests demonstrated the good water vapor hindering ability of the aerogel adsorbents. Comparison of the H_2O/CO_2 selectivity indicated that CO_2 was captured at a faster and more selective rate. The water vapor hindering ability of the aerogel adsorbents was demonstrated at the microscopic level using quantum chemical simulations·H_2O molecules are necessary for CO_2 adsorption; an appropriate amount of H_2O molecules promotes CO_2 adsorption, whereas excess H_2O hinders CO_2 adsorption. In summary, the aerogel adsorbents prepared by the freezing–ice-templating method were rich in pores, which provided CO_2 gas-phase mass transfer channels. The ultrahigh CO_2 adsorption kinetics of the adsorbents facilitated efficient CO_2 capture from ambient air. In addition, the aerogel adsorbents could be operated at medium humidity (50 %–80 % RH), which greatly broadens the scenarios and application conditions of moisture swing adsorbents and provides a strategy for CO_2 capture in humid environments.

CRediT authorship contribution statement

Hao Dong: Investigation, Formal analysis, Conceptualization, Methodology, Software, Data curation, Writing – original draft, Writing – review & editing. **Tao Wang:** Project administration, Supervision, Visualization, Writing – review & editing. **Fengsheng Liu:** Resources, Formal analysis, Methodology, Writing – review & editing. **Zhongyang Luo:** Resources, Writing – review & editing. **Xiang Gao:** Resources, Writing – review & editing. **Ming Cai:** Resources, Writing – review & editing.

Declaration of competing interest

The authors declare that they have no known competing financial interests or personal relationships that could have appeared to influence the work reported in this paper.

Data availability

Data will be made available on request.

Acknowledgments

This work was supported by the National Natural Science Foundation of China (No. 52276137), Fundamental Research Funds for the Central Universities (2022ZFJH004), R&D Program of Zhejiang Province, China (2023C03016), and Science and Technology Project of Xi'an Thermal Power Research Institute Co., Ltd. (TD-23-TYK01/H5).

Appendix A. Supplementary data

Supplementary data to this article can be found online at https://doi.org/10.1016/j.seppur.2024.129588.

References

[1] P. Siegmund, J. Abermann, O. Baddour, P. Canadell, A. Cazenave, C. Derksen, A. Garreau, S. Howell, M. Huss, K. Isensee, J. Kennedy, R. Mottram, R. Nitu, S. Ramasamy, K. Schoo, M. Sparrow, O. Tarasova, B. Trewin, M. Ziese, The Global Climate in 2015–2019, Switzerland, Geneva, 2019.
[2] X. Zhu, Y. Liu, M. Wang, L. Zhang, Q. Li, E. Zhang, H. Mo, Y. Gao, C. Xu, Y. Zhang, Boosting solar photothermal synergy for efficient overall water splitting based on Mg, Al codoped and Rh/Cr2O3/CoOOH coloaded SrTiO3, Chem. Eng. J. 479 (2024) 147636, https://doi.org/10.1016/j.cej.2023.147636.
[3] Intergovernmental Panel on Climate Change (IPCC). IPCC AR6 WGIII Final Draft Full Report, (2022).
[4] International Energy Agency (IEA). Direct Air Capture: A key technology for net zero, (2022).
[5] H. He, M. Zhong, D. Konkolewicz, K. Yacatto, T. Rappold, G. Sugar, N.E. David, J. Gelb, N. Kotwal, A. Merkle, K. Matyjaszewski, Three-Dimensionally Ordered Macroporous Polymeric Materials by Colloidal Crystal Templating for Reversible CO2 Capture, Adv. Funct. Mater. 23 (37) (2013) 4720–4728, https://doi.org/10.1002/adfm.201300401.
[6] T. Wang, X. Wang, C. Hou, J. Liu, Quaternary functionalized mesoporous adsorbents for ultra-high kinetics of CO2 capture from air, Sci. Rep. 10 (1) (2020), https://doi.org/10.1038/s41598-020-77477-1.
[7] J.V. Veselovskaya, V.S. Derevschikov, A.S. Shalygin, D.A. Yatsenko, K2CO3-containing composite sorbents based on a ZrO2 aerogel for reversible CO2 capture from ambient air, Microporous Mesoporous Mater. 310 (2021), https://doi.org/10.1016/j.micromeso.2020.110624.
[8] E.A. Recker, M. Green, M. Soltani, D.H. Paull, G.J. McManus, J.H. Davis, A. Mirjafari, Direct Air Capture of CO2 via Ionic Liquids Derived from "Waste" Amino Acids, ACS Sustain. Chem. Eng. 10 (36) (2022) 11885–11890, https://doi.org/10.1021/acssuschemeng.2c02883.
[9] M. Guo, H. Wu, L. Lv, H. Meng, J. Yun, J. Jin, J. Mi, A Highly Efficient and Stable Composite of Polyacrylate and Metal-Organic Framework Prepared by Interface Engineering for Direct Air Capture, ACS Appl. Mater. Interfaces 13 (18) (2021) 21775–21785, https://doi.org/10.1021/acsami.1c03661.
[10] G. Rim, F. Kong, M. Song, C. Rosu, P. Priyadarshini, R.P. Lively, C.W. Jones, Sub-Ambient Temperature Direct Air Capture of CO2 using Amine-Impregnated MIL-101(Cr) Enables Ambient Temperature CO2 Recovery, JACS Au 2 (2) (2022) 380–393, https://doi.org/10.1021/jacsau.1c00414.
[11] G. Rim, P. Priyadarshini, M. Song, Y. Wang, A. Bai, M.J. Realff, R.P. Lively, C. W. Jones, Support Pore Structure and Composition Strongly Influence the Direct

Air Capture of CO2 on Supported Amines, J. Am. Chem. Soc. 145 (13) (2023) 7190–7204, https://doi.org/10.1021/jacs.2c12707.
[12] G. Rim, T.G. Feric, T. Moore, A.H.A. Park, Solvent Impregnated Polymers Loaded with Liquid-Like Nanoparticle Organic Hybrid Materials for Enhanced Kinetics of Direct Air Capture and Point Source CO2 Capture, Adv. Funct. Mater. 31 (21) (2021), https://doi.org/10.1002/adfm.202010047.
[13] T. Wang, F. Liu, W. Tang, S. Xu, H. Dong, Z. Chen, X. Gao, Ultra-highly efficient adsorbent for CO2 capture from air by directional deprotonation regulation of MOFs-based amine grafting, Chem. Eng. J. 490 (2024), https://doi.org/10.1016/j.cej.2024.151426.
[14] D.W. Keith, G. Holmes, D. St, K.H. Angelo, A Process for Capturing CO2 from the Atmosphere, Joule 2 (8) (2018) 1573–1594, https://doi.org/10.1016/j.joule.2018.05.006.
[15] X. Zhu, T. Ge, F. Yang, R. Wang, Design of steam-assisted temperature vacuum-swing adsorption processes for efficient CO2 capture from ambient air, Renew. Sustain. Energy Rev. 137 (2021), https://doi.org/10.1016/j.rser.2020.110651.
[16] D.R. Kumar, C. Rosu, A.R. Sujan, M.A. Sakwa-Novak, E.W. Ping, C.W. Jones, Alkyl-Aryl Amine-Rich Molecules for CO2 Removal via Direct Air Capture, ACS Sustain. Chem. Eng. (2020), https://doi.org/10.1021/acssuschemeng.0c03706.
[17] Y. Yang, W. Liu, B. Wu, T. Wang, H. Dong, M. Fang, X. Gao, Kinetic research on ion exchange regeneration of quaternary ammonium-based CO2 sorbent for direct air capture, Sep. Purif. Technol. 324 (2023), https://doi.org/10.1016/j.seppur.2023.124504.
[18] T. Wang, X. Wang, H. Dong, K. Ge, K. Lackner, Moisture swing frequency response method for characterization of ion-transport kinetics of CO2 adsorption, Int. J. Heat Mass Transf. 216 (2023), https://doi.org/10.1016/j.ijheatmasstransfer.2023.124551.
[19] T.G. Feric, S.T. Hamilton, M.A. Haque, J. Jeddi, J. Sangoro, M.D. Dadmun, A.H. A. Park, Impacts of Bond Type and Grafting Density on the Thermal, Structural, and Transport Behaviors of Nanoparticle Organic Hybrid Materials-Based Electrolytes, Adv. Funct. Mater. 32 (36) (2022), https://doi.org/10.1002/adfm.202203947.
[20] O. Shekhah, Y. Belmabkhout, Z. Chen, V. Guillerm, A. Cairns, K. Adil, M. Eddaoudi, Made-to-order metal-organic frameworks for trace carbon dioxide removal and air capture, Nat. Commun. 5 (1) (2014), https://doi.org/10.1038/ncomms5228.
[21] S. Bose, D. Sengupta, T.M. Rayder, X. Wang, K.O. Kirlikovali, A.K. Sekizkardes, T. Islamoglu, O.K. Farha, Challenges and Opportunities: Metal-Organic Frameworks for Direct Air Capture, Adv. Funct. Mater. (2023), https://doi.org/10.1002/adfm.202307478.
[22] K.D. Kersey, G.A. Lee, J.H. Xu, M.K. Kidder, A.H.A. Park, Y.L. Joo, Encapsulation of Nanoparticle Organic Hybrid Materials within Electrospun Hydrophobic Polymer/Ceramic Fibers for Enhanced CO2 Capture, Adv. Funct. Mater. 33 (32) (2023), https://doi.org/10.1002/adfm.202301649.
[23] B. Thomas, S. Geng, J. Wei, H. Lycksam, M. Sain, K. Oksman, Ice-Templating of Lignin and Cellulose Nanofiber-Based Carbon Aerogels: Implications for Energy Storage Applications, ACS Applied Nano Materials 5 (6) (2022) 7954–7966, https://doi.org/10.1021/acsanm.2c01033.
[24] J. Song, J. Liu, W. Zhao, Y. Chen, H. Xiao, X. Shi, Y. Liu, X. Chen, Quaternized Chitosan/PVA Aerogels for Reversible CO2 Capture from Ambient Air, Ind. Eng. Chem. Res. 57 (14) (2018) 4941–4948, https://doi.org/10.1021/acs.iecr.8b00064.
[25] T. Wang, K.S. Lackner, A. Wright, Moisture Swing Sorbent for Carbon Dioxide Capture from Ambient Air, Environ. Sci. Tech. 45 (15) (2011) 6670–6675, https://doi.org/10.1021/es201180v.
[26] T. Wang, K.S. Lackner, A.B. Wright, Moisture-swing sorption for carbon dioxide capture from ambient air: a thermodynamic analysis, PCCP 15 (2) (2013) 504–514, https://doi.org/10.1039/c2cp43124f.
[27] C. Hou, Y. Wu, T. Wang, X. Wang, X. Gao, Preparation of Quaternized Bamboo Cellulose and Its Implication in Direct Air Capture of CO2, Energy Fuel 33 (3) (2018) 1745–1752, https://doi.org/10.1021/acs.energyfuels.8b02821.
[28] X. Kan, G. Zhang, J. Ma, F. Liu, Y. Tang, F. Liu, X. Yi, Y. Liu, A. Zheng, L. Jiang, F. S. Xiao, S. Dai, Multiscale Co-Assembly to Meso-Macroporous Foamed Single-Crystal Metal-Organic Frameworks for the Supported Capture of Sulfur Dioxide, Adv. Funct. Mater. 34 (19) (2024), https://doi.org/10.1002/adfm.202312044.
[29] J. Song, C. Chen, S. Zhu, M. Zhu, J. Dai, U. Ray, Y. Li, Y. Kuang, Y. Li, N. Quispe, Y. Yao, A. Gong, U.H. Leiste, H.A. Bruck, J.Y. Zhu, A. Vellore, H. Li, M.L. Minus, Z. Jia, A. Martini, T. Li, L. Hu, Processing bulk natural wood into a high-performance structural material, Nature 554 (7691) (2018) 224–228, https://doi.org/10.1038/nature25476.
[30] J. Li, C. Chen, J.Y. Zhu, A.J. Ragauskas, L. Hu, In Situ Wood Delignification toward Sustainable Applications, Accounts of Materials Research 2 (8) (2021) 606–620, https://doi.org/10.1021/accountsmr.1c00075.
[31] M. Kostag, T. Liebert, O.A. El Seoud, T. Heinze, Efficient Cellulose Solvent: Quaternary Ammonium Chlorides, Macromol. Rapid Commun. 34 (19) (2013) 1580–1584, https://doi.org/10.1002/marc.201300497.
[32] A. Pei, N. Butchosa, L.A. Berglund, Q. Zhou, Surface quaternized cellulose nanofibrils with high water absorbency and adsorption capacity for anionic dyes, Soft Matter 9(6) (2013). https://doi.org/10.1039/c2sm27344f.
[33] H. Dong, T. Wang, X. Wang, F. Liu, C. Hou, Z. Wang, W. Liu, L. Fu, X. Gao, Humidity sensitivity reducing of moisture swing adsorbents by hydrophobic carrier doping for CO2 direct air capture, Chem. Eng. J. 466 (2023) 143343, https://doi.org/10.1016/j.cej.2023.143343.
[34] J.C. Foster, I. Akar, M.C. Grocott, A.K. Pearce, R.T. Mathers, R.K. O'Reilly, 100th Anniversary of Macromolecular Science Viewpoint: The Role of Hydrophobicity in Polymer Phenomena, ACS Macro Lett. 9 (11) (2020) 1700–1707, https://doi.org/10.1021/acsmacrolett.0c00645.
[35] C.C. Bannan, G. Calabró, D.Y. Kyu, D.L. Mobley, Calculating Partition Coefficients of Small Molecules in Octanol/Water and Cyclohexane/Water, J. Chem. Theory Comput. 12 (8) (2016) 4015–4024, https://doi.org/10.1021/acs.jctc.6b00449.
[36] T. Lu, F. Chen, Multiwfn: A multifunctional wavefunction analyzer, J. Comput. Chem. 33 (5) (2011) 580–592, https://doi.org/10.1002/jcc.22885.
[37] H. Liimatainen, T. Suopajärvi, J. Sirviö, O. Hormi, J. Niinimäki, Fabrication of cationic cellulosic nanofibrils through aqueous quaternization pretreatment and their use in colloid aggregation, Carbohydr. Polym. 103 (2014) 187–192, https://doi.org/10.1016/j.carbpol.2013.12.042.
[38] C. Hou, D.R. Kumar, Y. Jin, Y. Wu, J.J. Lee, C.W. Jones, T. Wang, Porosity and hydrophilicity modulated quaternary ammonium-based sorbents for CO2 capture, Chem. Eng. J. 413 (2021) 127532, https://doi.org/10.1016/j.cej.2020.127532.
[39] F. Liu, T. Wang, H. Dong, W. Liu, Modified metal–organic framework by a novel coordinatively unsaturated amine grafting mechanism for direct air capture of CO2, Chem. Eng. J. 454 (2023) 140431, https://doi.org/10.1016/j.cej.2022.140431.
[40] L.A. Worku, M.G. Tadesse, A. Bachheti, D.P. Pandey, A.K. Chandel, A.W. Ewuntu, R.K. Bachheti, Experimental investigations on PVA/chitosan and PVA/chitin films for active food packaging using Oxytenanthera abyssinica lignin nanoparticles and its UV-shielding, antimicrobial, and antiradical effects, Int. J. Biol. Macromol. 254 (2024), https://doi.org/10.1016/j.ijbiomac.2023.127644.
[41] R.M. Parker, B. Frka-Petesic, G. Guidetti, G. Kamita, G. Consani, C. Abell, S. Vignolini, Hierarchical Self-Assembly of Cellulose Nanocrystals in a Confined Geometry, ACS Nano 10 (9) (2016) 8443–8449, https://doi.org/10.1021/acsnano.6b03355.
[42] W.K. Shi, X.J. Zhang, X. Liu, S. Wei, X. Shi, C. Wu, L. Jiang, Temperature-vacuum swing adsorption for direct air capture by using low-grade heat, J. Clean. Prod. 414 (2023) 137731, https://doi.org/10.1016/j.jclepro.2023.137731.
[43] R. Veneman, Z.S. Li, J.A. Hogendoorn, S.R.A. Kersten, D.W.F. Brilman, Continuous CO 2 capture in a circulating fluidized bed using supported amine sorbents, Chem. Eng. J. 207–208 (2012) 18–26, https://doi.org/10.1016/j.cej.2012.06.100.
[44] H.M. Schellevis, T.N. van Schagen, D.W.F. Brilman, Process optimization of a fixed bed reactor system for direct air capture, Int. J. Greenhouse Gas Control 110 (2021), https://doi.org/10.1016/j.ijggc.2021.103431.
[45] S. Chen, W.K. Shi, J.Y. Yong, Y. Zhuang, Q.Y. Lin, N. Gao, X.J. Zhang, L. Jiang, Numerical study on a structured packed adsorption bed for indoor direct air capture, Energy 282 (2023), https://doi.org/10.1016/j.energy.2023.128801.
[46] H. He, M. Zhong, D. Konkolewicz, K. Yacatto, T. Rappold, G. Sugar, N.E. David, K. Matyjaszewski, Carbon black functionalized with hyperbranched polymers: synthesis, characterization, and application in reversible CO2 capture, Journal of Materials Chemistry A 1(23) (2013). https://doi.org/10.1039/c3ta10699c.
[47] R. Foroutan, S.J. Peighambardoust, R. Mohammadi, S.H. Peighambardoust, B. Ramavandi, Cadmium ion removal from aqueous media using banana peel biochar/Fe3O4/ZIF-67, Environ. Res. 211 (2022), https://doi.org/10.1016/j.envres.2022.113020.
[48] J.C. Bullen, S. Saleesongsom, K. Gallagher, D.J. Weiss, A Revised Pseudo-Second-Order Kinetic Model for Adsorption, Sensitive to Changes in Adsorbate and Adsorbent Concentrations, Langmuir 37 (10) (2021) 3189–3201, https://doi.org/10.1021/acs.langmuir.1c00142.
[49] J. Wang, X. Guo, Adsorption kinetic models: Physical meanings, applications, and solving methods, J. Hazard. Mater. 390 (2020), https://doi.org/10.1016/j.jhazmat.2020.122156.
[50] T. Wang, C. Hou, K. Ge, K.S. Lackner, X. Shi, J. Liu, M. Fang, Z. Luo, Spontaneous Cooling Absorption of CO2 by a Polymeric Ionic Liquid for Direct Air Capture, The Journal of Physical Chemistry Letters 8 (17) (2017) 3986–3990, https://doi.org/10.1021/acs.jpclett.7b01726.
[51] T. Lu, Q. Chen, Shermo: A general code for calculating molecular thermochemistry properties, Comput. Theor. Chem. 1200 (2021), https://doi.org/10.1016/j.comptc.2021.113249.
[52] T. Wang, K. Ge, K. Chen, C. Hou, M. Fang, Theoretical studies on CO2 capture behavior of quaternary ammonium-based polymeric ionic liquids, PCCP 18 (18) (2016) 13084–13091, https://doi.org/10.1039/c5cp07229h.